Phenol-pyrazole ligands in the design of manganese(III) compounds : synthesis, structural characterization and study of the magnetic properties

Viciano Chumillas, Marta

Chapter 2

A family of mononuclear compounds: [Mn(HphpzR)$_2$X] (R = H, Me, Et, Ph; X$^-$ = Cl$^-$, Br$^-$)*

A series of mononuclear compounds was synthesized with the general formula of [Mn(HphpzR)$_2$X] (H_2phpzR = 3(5)-(2-hydroxyphenyl)-5(3)-R-pyrazole, R = H, Me, Et, Ph; X$^-$ = Cl$^-$, Br$^-$). All compounds are mononuclear manganese(III) coordination compounds in which the manganese(III) ion has a square-pyramidal geometry. The main difference arises from the crystal packing of the compounds which is caused by the ligand structure features. The influence of the ligand geometry is also reflected in the magnetic properties of the compounds.

* Part of this chapter has been published in the literature: Viciano-Chumillas M., Giménez-Marqués M., Tanase S., Evangelisti M., Mutikainen I., Turpeinen U., Smits J. M. M., de Gelder R., de Jongh L.J., Reedijk J., *J. Phys. Chem. C,* **2008**, 112, 20525–20534.

2.1. Introduction

Recently, polynuclear compounds have received considerable attention, since the field of molecular magnetism has greatly expanded due to the discovery of the single-molecule magnet (SMM) behaviour.[1-4] In synthetic respects, the search for novel SMM's with improved characteristic properties is rather complex and therefore the study of potential simple building blocks and their derivatives can be crucial for the design of SMM's. This can be illustrated by the studied manganese(III) salen complexes,[5] in which slight changes in simple molecules can lead to a better understanding of how to tune the magnetic properties, especially when dealing with the design of higher nuclearity compounds.[6,7]

Pyrazoles are very useful, functional bridging ligands, since they allow the connection of two metal ions by a variable superexchange pathway.[8,9] Substitutions in the heterocyclic ring can render novel ligands, providing a variety of coordination compounds.[10] In this respect, the ligand 3(5)-methyl-5(3)-(2-hydroxyphenyl)-pyrazole (H_2phpzMe) has exhibited a rich coordination chemistry with the introduction of a phenoxide moiety in the third position of the pyrazole ring providing another possible binding site with the metal ion.[11-13] Therefore, a library of phenol-pyrazole ligands, H_2phpzR (R = H, Me, Et, Ph) has now been synthesized with the purpose to study the structural effect of the substituent in the C5 position of the pyrazole ring (Scheme 2.1) on the magnetic properties of manganese(III) compounds. In this chapter, the synthesis, X-ray crystal structures, and magnetic and thermal properties are presented of a family of mononuclear manganese(III) compounds with the general formula [Mn(HphpzR)$_2$X] (R = H, Me, Et, Ph and X^- = Cl^-, Br^-). In these mononuclear compounds, the importance of the phenol-pyrazole derivatives is illustrated by the crystal packing and the magnetic properties. In addition, the influence of the different halogen on the magnetic properties has been studied.

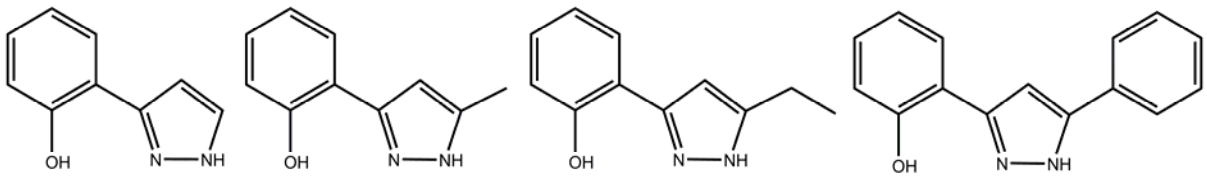

Scheme 2.1. Phenol-pyrazole based ligands (H_2phpzR; R = H, Me, Et, Ph) employed in this thesis.

2.2. Experimental Section

General remarks. Starting materials and the ligand 3(5)-(2-hydroxyphenyl)-pyrazole (H_2phpzH) were purchased from Aldrich and all manipulations were performed using materials as received.

Ligand synthesis

The ligands 3(5)-(2-hydroxyphenyl)-5(3)-methylpyrazole (H_2phpzMe), 3(5)-(2-hydroxyphenyl)-5(3)-ethylpyrazole (H_2phpzEt) and 3(5)-(2-hydroxyphenyl)-5(3)-phenylpyrazole (H_2phpzPh) have been synthesized according to reported procedures, by condensation of the 1,3-diketone derivatives[14-16] with hydrazine in refluxing alcohol (methanol or ethanol) (Scheme 2.2).[17]

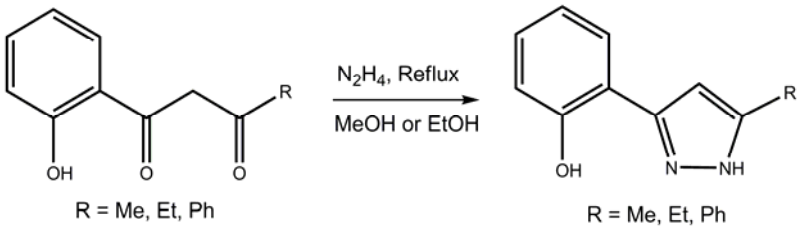

Scheme 2.2. H_2phpzR (R = Me, Et, Ph) ligand general synthesis.

General synthetic procedures for the coordination compounds

[Mn(HphpzR)$_2$Cl] (1, 3, 5, 7). $MnCl_2 \cdot 2H_2O$ (0.28 mmol) was dissolved in a mixture of acetonitrile/methanol in a ratio 1/1. The addition of a solution of H_2phpzH, H_2phpzMe, H_2phpzEt or H_2phpzPh (0.84 mmol) and triethylamine (0.14 mmol) in acetonitrile provided a green crystalline precipitate. The precipitate was collected by filtration, washed with diethyl ether and dried in vacuum. Green single crystals were obtained by slow evaporation of the filtrate in all four cases. Characterization details are given below.

[Mn(HphpzR)$_2$Br] (2, 4, 6, 8). The reaction of $MnBr_2 \cdot 4H_2O$ (0.28 mmol) in acetonitrile with a solution of H_2phpzH, H_2phpzMe, H_2phpzEt or H_2phpzPh (0.84 mmol) and triethylamine (0.14 mmol) in acetonitrile provided a green crystalline precipitate that was collected by filtration, washed with diethyl ether and dried in vacuum. The filtrate was allowed to slowly concentrate by evaporation, obtaining green single crystals in all four cases. Characterization details are given below.

[Mn(HphpzH)$_2$Cl] (1). Yield: 65% (77 mg). Anal. Calcd for **1** ($C_{18}H_{14}ClMnN_4O_2$): C, 52.90; H, 3.45; N, 13.71. Found: C, 52.35; H, 3.14; N, 13.68. IR (ν_{max}/cm^{-1}): 3260(m), 3055(w), 1602(s), 1563(m), 1520(s), 1505(s), 1469(m), 1442(s), 1436(s), 1362(m), 1314(m), 1294(s), 1248(s), 1173(s), 1143(s), 1115(vs), 1082(s), 1060(s), 1037(m), 974(m), 962(m),

924(m), 867(s), 852(s), 770(vs), 742(vs), 696(vs), 668(vs), 649(s), 586(vs), 572(vs), 533(vs), 468(vs), 448(s), 405(s), 369(s), 330(s), 313(s). ESI-MS (m/z): 405 $[Mn(HphpzH)_2(MeOH)]^+$, 373 $[Mn(HphpzH)_2]^+$. UV/VIS/NIR in solid state (λ_{max}, nm): 268, 302, 454, 676.

[Mn(HphpzH)$_2$Br] (2). Yield: 45% (57 mg). Anal. Calcd for **2** ($C_{18}H_{14}BrMnN_4O_2$): C, 47.71; H, 3.11; N, 12.36. Found: C, 46.93; H, 3.11; N, 12.32. IR (ν_{max}/cm^{-1}): 3287(m), 3054(w), 1602(s), 1563(m), 1520(s), 1505(s), 1496(s), 1468(m), 1443(s), 1436(s), 1361(w), 1313(m), 1297(s), 1246(vs), 1174(s), 1143(s), 1114(vs), 1082(s), 1058(s), 1036(m), 974(m), 964(m), 924(m), 868(s), 852(s), 772(vs), 745(vs), 689(vs),674(vs), 649(s), 582(vs), 573(vs), 534(w), 449(s), 406(s), 370(m), 314(s). ESI-MS (m/z): 405 $[Mn(HphpzH)_2(MeOH)]^+$, 373 $[Mn(HphpzH)_2]^+$. UV/VIS/NIR in solid state (λ_{max}, nm): 270, 377, 466, 674.

[Mn(HphpzMe)$_2$Cl] (3). Yield: 43% (53 mg). Anal. Calcd for **3** ($C_{20}H_{18}ClMnN_4O_2$): C, 55.00; H, 4.15; N, 12.83. Found: C, 55.12; H, 4.48; N, 12.98. IR (ν_{max}/cm^{-1}): 3331(m), 3056(w), 1602(s), 1570(m), 1558(s), 1511(w), 1456(s), 1310(s), 1283(s), 1244(vs), 1194(w), 1170(m), 1120(vs), 1069(s), 1043(m), 1028(m), 988(m), 868(vs), 784(vs), 749(vs), 722(s), 667(s), 648(vs), 596(s), 571(vs), 468(s), 397(vs), 354(vs), 338(s). ESI-MS (m/z): 433 $[Mn(HphpzMe)_2(MeOH)]^+$, 401 $[Mn(HphpzMe)_2]^+$. UV/VIS/NIR in solid state (λ_{max}, nm): 272, 378, 448, 678.

[Mn(HphpzMe)$_2$Br] (4). Yield: 50% (68 mg). Anal. Calcd for **4** ($C_{20}H_{18}ClMnN_4O_2$): C, 49.92; H, 3.77; N, 11.64. Found: C, 50.31; H, 4.09; N, 11.91. IR (ν_{max}/cm^{-1}): 3345(m), 3053(w), 1601(s), 1570(m), 1558(s), 1511(m), 1456(s), 1312(s), 1283(s), 1246(vs), 1194(m), 1174(s), 1120(vs), 1070(s), 1043(s), 1028(m), 988(m), 970(w), 932(w), 871(s), 785(vs), 766(s), 758(m), 746(vs), 722(vs), 690(s), 678(m), 656(vs), 646(vs), 607(m), 570(vs), 535(m), 464(s), 398(s), 348(s). ESI-MS (m/z): 433 $[Mn(HphpzMe)_2(MeOH)]^+$, 401 $[Mn(HphpzMe)_2]^+$. UV/VIS/NIR in solid state (λ_{max}, nm): 272, 381, 458, 694. During the crystallization process of **4**, a second minor product was characterized only crystallographically as $[Mn(HphpzMe)_2(H_2phpzMe)_2]Br$ (**9**).

[Mn(HphpzEt)$_2$Cl] (5). Yield: 34% (44 mg). Anal. Calcd for **5** ($C_{22}H_{22}ClMnN_4O_2$): C, 56.85; H, 4.77; N, 12.05. Found: C, 56.73; H, 5.49; N, 12.11. IR (ν_{max}/cm^{-1}): 3308(m), 3054(w), 1601(s), 1568(m), 1558(s), 1554(s), 1540(m), 1506(m), 1476(s), 1448(vs), 1436(s), 1341(m), 1303(s), 1275(m), 1246(vs), 1172(m), 1117(vs), 1072(s), 1042(s), 1030(m), 993(m), 946(w), 861(vs), 804(vs), 758(vs), 714(m), 672(vs), 647(vs), 638(vs), 603(s), 570(vs), 541(m), 483(m), 469(w), 430(m), 391(m), 370(w), 336(s). ESI-MS (m/z): 461 $[Mn(HphpzEt)_2(MeOH)]^+$, 429 $[Mn(HphpzEt)_2]^+$. UV/VIS/NIR in solid state (λ_{max}, nm): 271, 348, 446, 669.

[Mn(HphpzEt)$_2$Br] (6). Yield: 30% (43 mg). Anal. Calcd for **6** ($C_{22}H_{22}BrMnN_4O_2$): C, 51.88; H, 4.35; N, 11.00. Found: C, 51.79; H, 4.22; N, 11.20. IR (ν_{max}/cm^{-1}): 3324(m), 3054(w), 1601(s), 1568(m), 1558(s), 1554(s), 1540(w), 1506(w), 1472(s), 1447(vs), 1436(s), 1398(w), 1377(w), 1343(m), 1308(s), 1278(s), 1245(vs), 1174(s), 1116(vs), 1074(s), 1042(s), 1031(m), 992(m), 936(w), 860(vs), 802(vs), 748(vs), 710(m), 689(m), 651(vs), 586(s), 565(vs), 474(m), 426(s), 388(s), 336(s). ESI-MS (m/z): 461 [Mn(HphpzEt)$_2$(MeOH)]$^+$, 429 [Mn(HphpzEt)$_2$]$^+$. UV/VIS/NIR in solid state (λ_{max}, nm): 272, 385, 446, 690.

[Mn(HphpzPh)$_2$Cl]·CH$_3$CN (7). Yield: 53% (90 mg). Anal. Calcd for **7** ($C_{32}H_{25}ClMnN_5O_2$): C, 63.85; H, 4.19; N, 11.63. Found: C, 63.41; H, 4.08; N, 11.51. IR (ν_{max}/cm^{-1}): 3367(m), 3040(vw), 1600(s), 1557(m), 1510(w), 1488(s), 1472(s), 1456(s), 1443(w), 1418(m), 1398(m), 1302(m), 1246(vs), 1198(m), 1126(vs), 1062(m), 1039(s), 994(s), 862(vs), 826(m), 804(m), 757(vs), 706(s), 690(vs), 676(m), 665(vs), 647(m), 618(w), 582(vs), 513(m), 466(m), 448(s) 403(w), 373(s), 334(vs). ESI-MS (m/z): 566 [Mn(HphpzPh)$_2$(CH$_3$CN)]$^+$, 557 [Mn(HphpzPh)$_2$(MeOH)]$^+$, 525 [Mn(HphpzPh)$_2$]$^+$. UV/VIS/NIR in solid state (λ_{max}, nm): 299, 392, 453, 695.

[Mn(HphpzPh)$_2$Br]·CH$_3$CN (8). Yield: 46% (83 mg). Anal. Calcd for **8** ($C_{32}H_{25}BrMnN_5O_2$): C, 59.46; H, 3.90; N, 10.83. Found: C, 59.95; H, 4.35; N, 10.97. IR (ν_{max}/cm^{-1}): 3367(m), 3040(vw), 1600(s), 1557(m), 1510(s), 1488(s), 1472(s), 1455(s), 1443(m), 1418(m), 1396(m), 1301(m), 1245(vs), 1198(m), 1152(w), 1126(vs), 1062(m), 1039 (s), 994(s), 935(w), 920(w), 862(vs), 823(m), 805(m), 774(w), 756(vs), 708(s), 688(vs), 676(s), 666(vs), 648(s), 618(w), 582(vs), 512(m), 486(w), 466(m), 449(s) 410(w), 375(m), 334(vs), 314(w). ESI-MS (m/z): 566 [Mn(HphpzPh)$_2$(CH$_3$CN)]$^+$, 557 [Mn(HphpzPh)$_2$(MeOH)]$^+$, 525 [Mn(HphpzPh)$_2$]$^+$. UV/VIS/NIR in solid state (λ_{max}, nm): 298, 396, 458, 696.

Physical Measurements. Elemental analysis for C, H and N were performed on a Perkin-Elmer 2400 series II analyzer. Infrared spectra (4000–300 cm^{-1}) were recorded on a Perkin-Elmer Paragon 1000 FTIR spectrometer equipped with a Golden Gate ATR device, using the reflectance technique. Electronic absorption spectra were obtained on a Perkin-Elmer Lambda 900 spectrophotometer, using the diffuse reflectance technique, with MgO as a reference. Electrospray mass spectra (ESI-MS) in methanol solution were recorded on a Thermo Finnigan AQA apparatus. DC magnetic data were recorded using a Quantum Design MPMS-5 SQUID susceptometer. The magnetic susceptibilities were measured from 1.8 to 300 K on polycrystalline samples in a gelatine capsule with an applied field of 0.1 T. The magnetization was measured at 2, 4, 6 and 20 K in the 0–5(7) T range. Data were corrected for magnetization of the sample holder and for diamagnetic contributions, which were

estimated from Pascal's constants.[18] Specific heat measurements in zero field were carried out in the range 0.3 K to 20 K with a commercial ^{3}He set-up (PPMS), using the relaxation method. The investigated samples were in the form of microcrystalline powders.

X-ray Crystallography. Intensity data for single crystals of **2**, **3**, **7**, **8** and **9** were collected using MoKα radiation (λ = 0.71073 Å) on a Nonius KappaCCD diffractometer. Crystal and refinement data for **2**, **3**, **7** and **8** are collected in Table 2.1. The intensity data were corrected for Lorentz and polarization effects, and for absorption (multiscan absorption correction[19]). The structures were solved by Patterson methods.[20] The programs EvalCCD,[21,22] DIRDIF96,[23] SHELXS–97[24] and SHELXL–97[25] were used for data reduction, structure solution and refinement respectively. All non-hydrogen atoms were refined with anisotropic displacement parameters. All hydrogen atoms were placed at calculated positions and were refined riding on their parent atoms.

2.3. Results and Discussion

Synthesis and General Characterization. The reaction between $MnX_2 \cdot nH_2O$ (X^- = Cl^-, Br^-) and H_2phpzR (R = H, Me, Et, Ph) in the presence of a small quantity of base in acetonitrile affords the compounds with the general formula $[Mn(HphpzR)_2X]$. In the case of the manganese(II) chloride, methanol should be added to improve the solubility of the salt. This family of compounds contains the manganese(III) ion, formed by aerial oxidation upon stirring the manganese(II) salt. The reactions can also be performed in the stoichiometric ratio 1 to 2 (metal to ligand), but the yields do not change significantly compared with the described procedures. During the crystallization process of compound **4**, some secondary product was characterized crystallographically as $[Mn(HphpzMe)_2(H_2phpzMe)_2]Br$ (**9**). Probably the excess of the ligand in solution has rendered this new complex.

The infrared spectra of the compounds **1**–**8** display sharp bands in the range of 3260–3368 cm^{-1} which belong to the ν_{N-H} stretching vibrations. Several weak bands are observed in the range of 2900–3100 cm^{-1} due to the ν_{C-H} of the aromatic rings. The ν_{C-O} and $\nu_{C=N}$ stretching vibrations are shifted to lower energies, around 1602 and 1560 cm^{-1}, for compounds **1**–**8** as compared to the free ligand, indicating the coordination of the H_2phpzR ligand. This fact is also supported by the absence of any band in the range 3300−3600 cm^{-1} from the protonated phenolic group.[26]

In the electronic absorption spectra of compounds **1**–**8**, a broad band with the maximum in the range of 670–700 nm is observed, which is ascribed to a d–d transition of the manganese(III) ion.[27] The band with shoulders in the range of 300–470 nm is assigned to

LMCT transitions. The absorption bands around 265–300 nm belong to the π–π* transitions within the ligand because of their high intensity.[27,28]

The positive ESI-MS spectrum of a methanol solution of the compounds **1**–**8** exhibits two prominent signals that are assigned to the fragments $[Mn(HphpzR)_2(MeOH)]^+$ and $[Mn(HphpzR)_2]^+$. Compounds **7** and **8** also show the fragment $[Mn(HphpzPh)_2(CH_3CN)]^+$. The good solubility of these compounds in methanol and the empty positions at the coordination sphere led to use these compounds as starting materials to obtain trinuclear manganese(III) clusters (see Chapter 3).[29] Compounds **1**, **4**, **5** and **6** were not characterized by X-ray crystallography. However, all the analyses performed on **1** and **4** indicate their isostructurality with the compounds **2** and **3**, respectively. In addition, the analysis of **5** and **6** also agrees with the formation of the mononuclear compounds, $[Mn(HphpzEt)_2X]$ (X^- = Cl^-, Br^-).

Description of the Molecular Structures. Compounds **2**, **3**, **7** and **8** consist of a manganese(III) ion with a square-pyramidal N_2O_2X chromophore (X^- = Cl^-, Br^-), where the two phenol-pyrazole ligands form the basal plane and the halogen is at the apical position. Figure 2.1 shows the molecular structure of compound **2**. In all compounds, the square-pyramidal geometry is thermodynamically favoured above the well known octahedral-based geometry for a manganese(III) ion, probably due to the formation of the neutral molecular compounds.[30] Nevertheless, a complex with octahedral geometry can also be formed in the presence of an excess of ligand as illustrated by the formation of compound **9** (Figure 2.2). In compounds **7** and **8**, the unit cell consists of two independent $[Mn(HphpzPh)_2X]$ (X^- = Cl^- (**7**), Br^- (**8**)) units and two molecules of acetonitrile as the Figure 2.3 shows for compound **7**.

All compounds crystallize in the triclinic space group P−1, except compound **9** which crystallizes in the monoclinic space group $P2_1/c$. The coordination geometry for compounds **2**, **3**, **7** and **8** is square-pyramidal with the value for τ in the range 0.02–0.16 (τ = 0 for perfect square-pyramidal geometry and τ = 1 for trigonal bipyramidal geometry).[31] Compound **9** exhibits a distorted octahedral geometry with two mono deprotonated $HphpzMe^-$ ligands in the equatorial plane (Mn(1)–O(10) = 1.885(3) Å and Mn(1)–N(21) = 2.012(4) Å). The axial positions are occupied by two nitrogen atoms of two neutral $H_2phpzMe$ ligands, which display an elongated Jahn-Teller axis typical for manganese(III) ion (Mn(1)–N(45) = 2.343(4) Å). The intramolecular hydrogen bonds involve the O(phenol)–H and N(pz)–H moieties. Intermolecular hydrogen bonds are present between the phenoxide moiety and the counterion, the bromide atom (Figure 2.2b and Table 2.4). The Mn–O average bond lengths are 1.85 Å, 1.85 Å, 1.86 Å and 1.87 Å for compounds **2**, **3**, **7** and **8**, respectively, while the Mn–N

average bond lengths are 1.97 Å, 2.02 Å, 1.99 Å and 1.99 Å for compounds **2**, **3**, **7** and **8**. The Mn–X bond is longer in the case of compounds **2** (2.60 Å) and **8** (av. 2.54 Å) than in the compounds **3** (2.41 Å) and **7** (av. 2.38 Å), which is ascribed to the smaller ionic radius and larger electronegativity of the Cl^- anion as compared with Br^-. This is also reflected in the distortion of the coordination geometry, where the distances of the manganese(III) ion from the plane formed by N_2O_2 are 0.272 Å and 0.312 Å for **2**, **3** respectively, and 0.337 Å for Mn(1) and 0.371 Å for Mn(2) in compound **7**, and 0.311 Å for Mn(1) and 0.343 Å for Mn(2) in compound **8**. Selected distances and angles are listed in Tables 2.2 and 2.3 for compounds **2**, **3**, **7** and **8**. The angles O–Mn–N are slightly smaller than 90º for all compounds. The dihedral angles between the phenol and the pyrazole ring are: 8.30º and 9.98º in compound **2**; 4.15º and 6.72º for Mn(1) and 5.05º and 7.42º for Mn(2) in compound **7**; and 3.92º and 7.93º for Mn(1) and 5.00º and 8.02º for Mn(2) in compound **8**. These values indicate nearly planar systems, as opposed to **3** for which values of 3.79º and 13.01º have been found as a result of the stronger distortion imposed by the ligand.

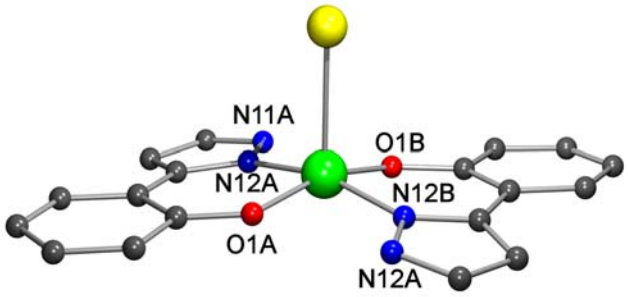

Figure 2.1. Pluton projection of the molecular structure of $[Mn(HphpzH)_2Br]$ (**2**). Hydrogen atoms are omitted for clarity. Colour code: green, manganese; yellow, bromide; blue, nitrogen; red, oxygen; grey, carbon.

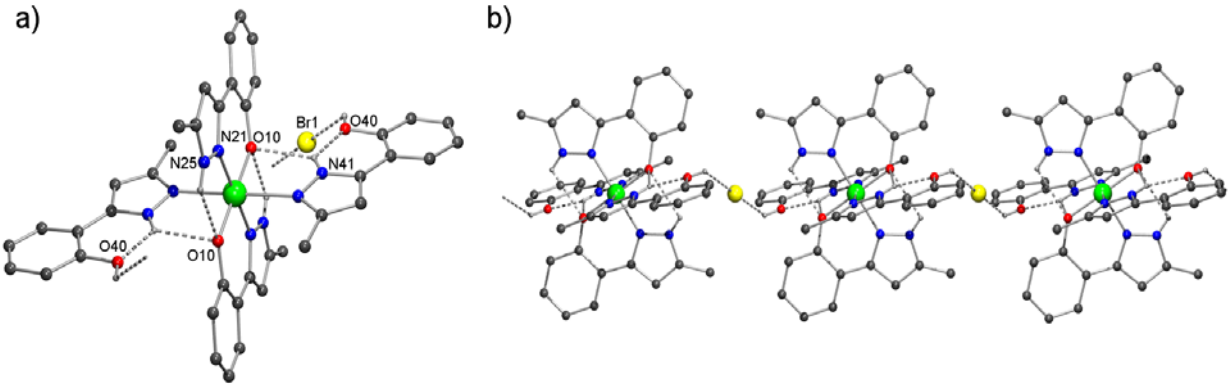

Figure 2.2. Pluton projection of the molecular structure of $[Mn(HphpzMe)_2(H_2phpzMe)_2]Br$ (**9**) (a) showing the hydrogen bonding interactions (b). Hydrogen atoms that are not involved in hydrogen bonds are omitted for clarity. Colour code: green, manganese; yellow, bromide; blue, nitrogen; red, oxygen; grey, carbon.

Table 2.1. Crystal data and structure refinements for **2**, **3**, **7**, **8** and **9**.

	2	**3**	**7**	**8**	**9**
Formula	$C_{18}H_{14}BrMnN_4O_2$	$C_{20}H_{18}ClMnN_4O_2$	$C_{32}H_{25}ClMnN_5O_2$	$C_{32}H_{25}BrMnN_5O_2$	$C_{40}H_{38}BrMnN_8O_4$
Formula weight [$gmol^{-1}$]	453.17	436.77	601.96	646.41	829.62
Crystal system	Triclinic	Triclinic	Triclinic	Triclinic	Monoclinic
Space group	P–1	P–1	P−1	P−1	$P2_1/c$
a [Å]	8.6761(10)	8.7790(18)	10.856(2)	10.812(2)	11.349(2)
b [Å]	9.3331(7)	10.361(2)	13.678(2)	13.893(3)	18.919(4)
c [Å]	11.2913(5)	11.622(2)	20.542(4)	20.995(4)	8.6560(17)
α [º]	91.992(5)	109.93(3)	88.93(3)	89.26(3)	90
β [º]	104.378(6)	90.73(3)	79.77(3)	79.51(3)	91.53(3)
γ [º]	105.636(6)	108.35(3)	70.75(3)	70.56(3)	90
V [$Å^3$]	847.82(13)	934.7(4)	2831.3(11)	2920.3(12)	1857.9(6)
Z	2	2	4	4	2
D_{calc} [gcm^{-3}]	1.7752	1.552	1.412	1.470	1.483
Crystal size	0.07×0.18×0.29	0.05×0.05×0.10	0.02×0.08×0.40	0.02×0.06×0.40	0.11×0.30×0.30
Number of collected reflections (unique)	26394(3889)	13915(4256)	34068(12486)	37936(12953)	22018(4214)
Number of observed reflections [$I_o > 2\sigma(I_o)$]	3078	2825	7391	6351	2018
Internal R factor	0.041	0.069	0.085	0.111	0.104
Number of parameters	235	253	741	741	247
Goodness-of-fit S on F^2	1.12	1.04	1.06	1.01	1.07
Largest peak and hole in final difference Fourier map [e $Å^{-3}$]	0.960 and −0.40	0.69 and −1.13	0.57 and −0.88	0.58 and −1.11	1.28 and −1.09
μ [mm^{-1}]	3.156	0.874	0.600	1.858	1.483
R_1 [a] [$I > 2.0\sigma(I)$]	0.0363	0.0588	0.0594	0.0631	0.0750
wR_2 [b] [all data]	0.0834	0.1803	0.1612	0.1783	0.2467
T [ºC]	208	173	173	173	173

[a] $R_1 = \sum||F_o| - |F_c|| / \sum|F_o|$. [b] $wR_2 = \{\sum[w(F_o^2 - F_c^2)^2]/\sum w(F_o^2)^2\}^{1/2}$.

The crystal packing of compounds **2** (Figure 2.4) and **3** is similar. The molecules align face-to-face to form ladder-like chains resulting from the intermolecular hydrogen bonds between the halogen ion from one molecule and the N–H group from the pyrazole ring of the next molecule. In case of the compound **3**, the hydrogen-bond interactions (N(45)–H(45A)···Cl(1) = 3.545(4) Å and N(25)–H(255A)···Cl(1) = 3.694(5) Å) are weaker than in the case of **2** (N(11A)–H(11A)···Br(1) = 3.289(3) Å and N(11B)–H(11B)···Br(1) = 3.304(3) Å), which is ascribed to the steric effect of the methyl moiety that increases the separation between mononuclear manganese(III) units. Hydrogen bond details are listed in Table 2.4 for compounds **2** and **3**. The "intrachain" Mn···Mn distances are 5.908 and 5.999 Å and the shortest "interchain" Mn···Mn distance is 5.179 Å for **2**. In the case of compound **3**, the "intrachain" Mn···Mn distances are 5.946 and 6.305 Å and the shortest "interchain" Mn···Mn distance is 5.832 Å.

Table 2.2. Selected bond lengths [Å] and angles [º] for [Mn(HphpzH)$_2$Br] (**2**) and [Mn(HphpzMe)$_2$Cl] (**3**).

Compound **2**					
Bond Lengths					
Mn(1)–Br(1)	2.6025(6)	Mn(1)–O(1A)	1.8460(19)	Mn(1)–N(12B)	1.9628(26)
Mn(1)–O(1B)	1.8487(19)	Mn(1)–N(12A)	1.9692(25)		
Bond Angles					
Br(1)–Mn(1)–O(1A)	98.70(6)	Br(1)–Mn(1)–O(1B)	98.75(6)	Br(1)–Mn(1)–N(12B)	98.14(8)
O(1A)–Mn(1)–O(1B)	162.55(9)	O(1A)–Mn(1)–N(12A)	89.20(10)		
Compound **3**					
Bond Lengths					
Mn(1)–Cl(1)	2.4129(13)	Mn(1)–O(10)	1.851(3)	Mn(1)–N(21)	2.022(3)
Mn(1)–O(30)	1.857(3)	Mn(1)–N(41)	2.026(3)		
Bond Angles					
Cl(1)–Mn(1)–O(10)	98.05(10)	Cl(1)–Mn(1)–O(30)	98.26(10)	Cl(1)–Mn(1)–N(21)	102.07(11)
Cl(1)–Mn(1)–N(41)	98.44(11)	O(10)–Mn(1)–O(30)	163.69(13)	O(10)–Mn(1)–N(21)	89.14(13)
O(10)–Mn(1)–N(41)	89.05(13)				

The packing diagram of compounds **7** and **8** differs from that of **2** and **3**, due to the presence of two crystallographically independent mononuclear units and two acetonitrile molecules in the unit cell. The two independent manganese(III) units have different orientations, where the angle between the N_2O_2 plane of the units is 56.94º and 56.39º for compounds **7** and **8**, respectively (Figure 2.3). One acetonitrile molecule forms an intermolecular hydrogen bond that involves its N(4) atom and N(25)–H function of one of the ligands coordinated to Mn(1) with a N–H···N distance of 3.040 Å and 3.069 Å for compounds **7** and **8**, respectively. In addition, intramolecular hydrogen bonds are present between the

N−H of the pyrazole ring and the O of the phenoxide moiety. In Figure 2.5, the packing of compound **8** is shown. The presence of the two units with different orientation derivates in two layers, namely **I** (formed by the mononuclear entities containing Mn(1)) and **II** (formed by the mononuclear units containing Mn(2)). One acetonitrile molecule is found into the layer **I** and the other acetonitrile molecule lies between the layers **I** and **II**. Within the layers, the mononuclear entities align face-to-face although no direct interactions between the mononuclear units are observed. The shortest intermolecular face-to-face Mn···Mn distances are 7.793 Å (Mn(1)···Mn(1)) and 7.344 Å (Mn(2)···Mn(2)) for compound **7**, and 7.905 Å (Mn(1)···Mn(1)) and 7.433 Å (Mn(2)···Mn(2)) for compound **8**, respectively. However, the closest distance between manganese(III) ions belongs to the manganese(III) ions that are opposite to each other, corresponding to 5.660 Å and 5.502 Å (Mn(2)···Mn(2)) for compounds **7** and **8**, respectively.

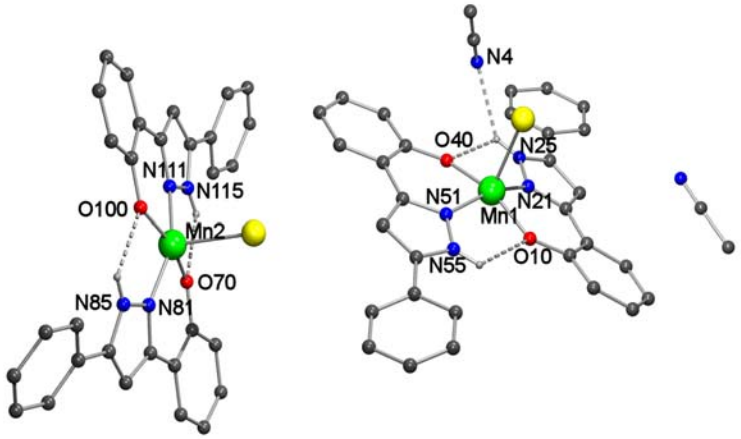

Figure 2.3. Pluton projection of the unit cell of the compound $[Mn(HphpzPh)_2Br]\cdot CH_3CN$ (**8**) showing the two independent molecules and the hydrogen-bonding interactions. Hydrogen atoms that are not involved in hydrogen bonds are omitted for clarity. Colour code: green, manganese; yellow, bromide; blue, nitrogen; red, oxygen; grey, carbon.

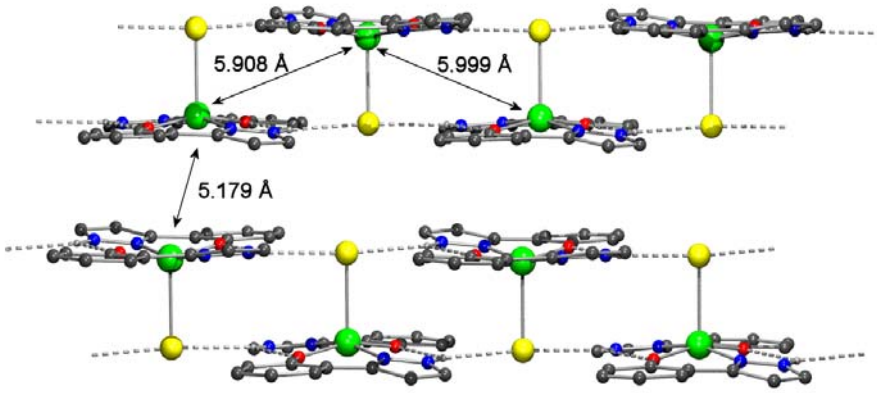

Figure 2.4. View of the ladder-like chain of [Mn(HphpzH)Br] (**2**) showing the intramolecular and intermolecular hydrogen bonds N–H···Br···N–H.

Table 2.3. Selected bond lengths [Å] and angles [º] for $[Mn(HphpzPh)_2Cl]\cdot CH_3CN$ (**7**) and $[Mn(HphpzPh)_2Br]\cdot CH_3CN$ (**8**).

Compound **7**					
Bond Lengths					
Mn(1)−Cl(1)	2.3889(13)	Mn(1)−O(10)	1.864(3)	Mn(1)−N(21)	2.003(3)
Mn(1)−O(40)	1.857(3)	Mn(1)−N(51)	1.991(3)	Mn(2)−Cl(2)	2.3784(14)
Mn(2)−N(81)	1.983(3)	Mn(2)−O(70)	1.861(3)	Mn(2)−N(111)	1.991(3)
Mn(2)−O(100)	1.867(3)				
Bond Angles					
O(10)−Mn(1)−O(40)	161.55(13)	N(21)−Mn(1)−N(51)	158.28(13)	O(40)−Mn(1)−N(21)	88.35(12)
Cl(1)−Mn(1)−O(40)	100.17(10)	O(10)−Mn(1)−N(21)	89.18(13)	Cl(1)−Mn(1)−O(10)	98.25(10)
O(40)−Mn(1)−N(51)	88.17(13)	Cl(1)−Mn(1)−N(21)	101.09(10)	O(10)−Mn(1)−N(51)	87.39(12)
Cl(1)−Mn(1)−N(51)	100.63(10)	O(70)−Mn(2)−O(100)	162.91(13)	N(81)−Mn(2)−N(111)	152.97(13)
O(70)−Mn(2)−N(81)	88.69(13)	Cl(2)−Mn(2)−O(70)	99.22(10)	O(100)−Mn(2)−N(81)	87.37(12)
Cl(2)−Mn(2)−O(100)	97.85(10)	O(70)−Mn(2)−N(111)	87.96(13)	Cl(2)−Mn(2)−N(81)	106.35(10)
O(100)−Mn(2)−N(111)	88.01(13)	Cl(2)−Mn(2)−N(111)	100.66(10)		
Compound **8**					
Bond Lengths					
Mn(1)−Br(1)	2.5441(12)	Mn(1)−O(10)	1.875(4)	Mn(1)−N(21)	1.994(4)
Mn(1)−O(40)	1.870(4)	Mn(1)−N(51)	2.001(4)	Mn(2)−Br(2)	2.5447(11)
Mn(2)−N(81)	1.986(4)	Mn(2)−O(70)	1.869(4)	Mn(2)−N(111)	1.999(4)
Mn(2)−O(100)	1.871(4)				
Bond Angles					
O(10)−Mn(1)−O(40)	162.22(18)	N(21)−Mn(1)−N(51)	160.71(18)	O(40)−Mn(1)−N(21)	88.61(18)
Br(1)−Mn(1)−O(40)	99.52(13)	O(10)−Mn(1)−N(21)	89.58(18)	Br(1)−Mn(1)−O(10)	98.22(12)
O(40)−Mn(1)−N(51)	88.74(17)	Br(1)−Mn(1)−N(21)	99.65(13)	O(10)−Mn(1)−N(51)	87.16(17)
Br(1)−Mn(1)−N(51)	99.63(13)	O(70)−Mn(2)−O(100)	163.33(16)	N(81)−Mn(2)−N(111)	155.94(18)
O(70)−Mn(2)−N(81)	89.18(17)	Br(2)−Mn(2)−O(70)	97.81(11)	O(100)−Mn(2)−N(81)	87.39(17)
Br(2)−Mn(2)−O(100)	98.83(11)	O(70)−Mn(2)−N(111)	88.37(17)	Br(2)−Mn(2)−N(81)	105.40(13)
O(100)−Mn(2)−N(111)	88.14(17)	Br(2)−Mn(2)−N(111)	98.65(12)		

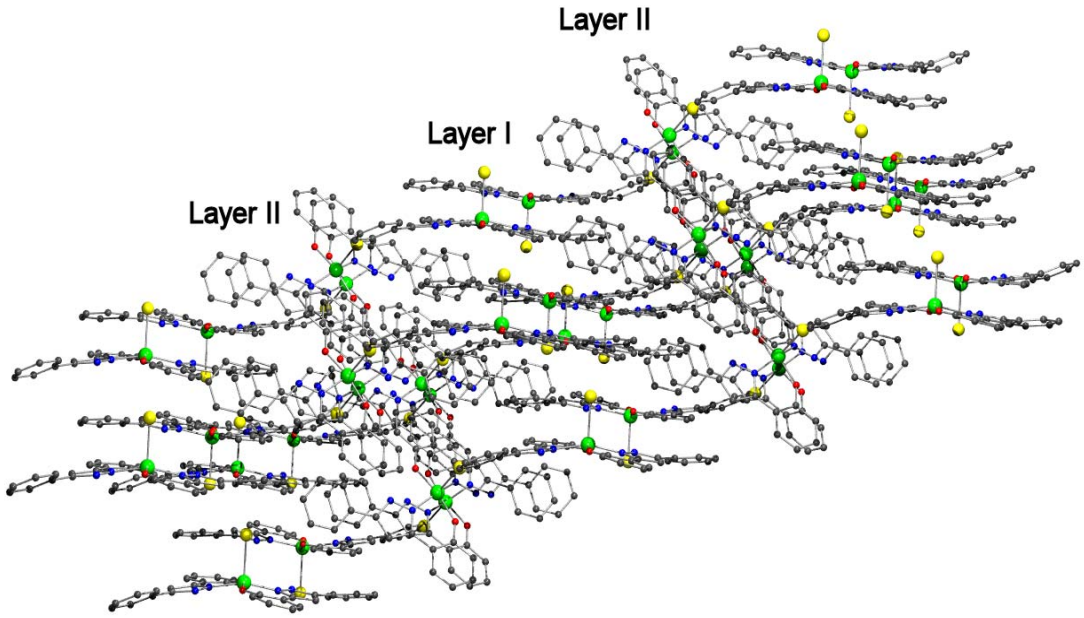

Figure 2.5. View of the 3-D network of $[Mn(HphpzPh)_2Br]\cdot CH_3CN$ (**8**). Hydrogen atoms and acetonitrile molecules are omitted for clarity.

Table 2.4. Hydrogen bond details (lengths [Å] and angles [º]) for $[Mn(HphpzH)_2Br]$ (**2**), $[Mn(HphpzMe)_2Cl]$ (**3**) and $[Mn(HphpzMe)_2(H_2phpzMe)_2]Br$ (**9**).

Donor–H···Acceptor	D–H	H···A	D···A	D–H···A
Compound **2**				
N(11A)–H(11A)···O(1B)	0.8696	2.3695	2.774(3)	108.72
N(11A)–H(11A)···Br(1)	0.8696	2.5931	3.289(3)	137.68
N(11B)–H(11B)···O(1A)	0.8701	2.3631	2.774(3)	109.22
N(11B)–H(11B)···Br(1)	0.8701	2.5974	3.304(3)	139.05
Compound **3**				
N(25)–H(25A)···O(30)	0.8797	2.4176	2.819(4)	108.20
N(45)–H(45A)···O(10)	0.8801	2.4967	2.889(4)	107.70
N(45)–H(45A)···Cl(1)	0.8801	2.7718	3.545(4)	147.44
N(25)–H(25A)···Cl(1)	0.8797	2.9428	3.694(5)	144.50
Compound **9**				
N(25)–H(25A)···O(10)	0.8800	2.4927	2.906(6)	109.40
O(30)–H(301)···Br(1)	0.8404	2.6172	3.151(4)	122.64
N(41)–H(41A)···O(10)	0.8795	2.2809	2.842(5)	121.53
N(41)–H(41A)···O(30)	0.8795	1.9676	2.589(6)	126.48

Magnetic Properties. Magnetic susceptibilities were measured under 0.1 T applied field in the 1.8–300 K temperature range for all compounds except **9**. The $\chi_M T$ values found at 300 K are seen to be in the range 2.7–2.9 cm^3Kmol^{-1}, values which are slightly below the theoretical value (3.0 cm^3Kmol^{-1}) expected for non-interacting manganese(III) ions with $S = 2$ and $g = 2$. Upon cooling to 2 K, the $\chi_M T$ values for all the compounds **1**–**8** decrease considerably, suggesting predominantly antiferromagnetic interactions between the manganese(III) ions along the structural chains (for compounds **1**–**4**) and between nearest neighbours (for compounds **7** and **8**). This conclusion is corroborated by magnetization measurements taken at low temperature (< 20 K). In all cases the field-dependent magnetization curves show substantial downward deviations from the calculated Brillouin curves for non-interacting spins, as will be further discussed below.

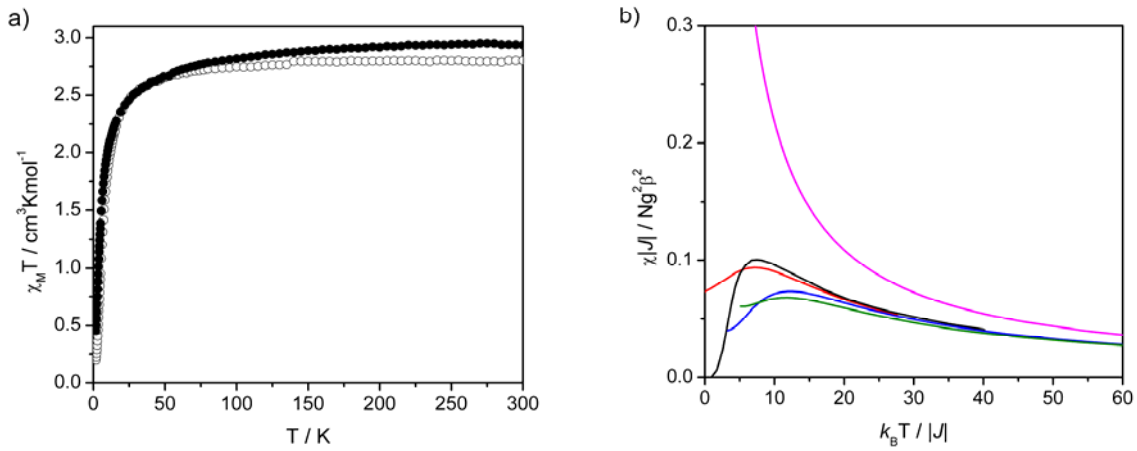

Figure 2.6. a) Plot of $\chi_M T$ *vs* T for **1** (○) and **2** (●) in the range 1.8 to 300 K in 0.1 T applied field. b) Plot of $\chi_M|J|/Ng^2\beta^2$ *vs* $k_BT/|J|$ for **1** (blue) and **2** (green) together with the theoretical predictions for Heisenberg (red) and Ising (black) chains for $S = 2$ and the paramagnet behaviour (magenta).

Compounds 1 and 2. Interestingly, compounds **1** and **2** both exhibit a broad maximum in the susceptibility plot at 7 K and at 4 K, respectively (Figure 2.6b), which is a characteristic feature of antiferromagnetic linear chains.[18,32] The increasing development of antiferromagnetic correlations along the chains as temperature is lowered is known to lead to broad maxima in the magnetic susceptibility and specific heat at temperatures of the order of the magnetic exchange constant.[33] These two compounds were therefore further investigated by specific heat measurements in the temperature range 0–20 K and in zero magnetic field (Figure 2.8). Since the measured specific heat is the sum of a magnetic (C_m) and a lattice (phonon) contribution (C_l), the latter has to be evaluated and subtracted from the raw data. At low temperature C_l can be well approximated by a temperature polynomial of the form:[34]

$$C_l = aT^3 + bT^5 + cT^7 \quad (1)$$

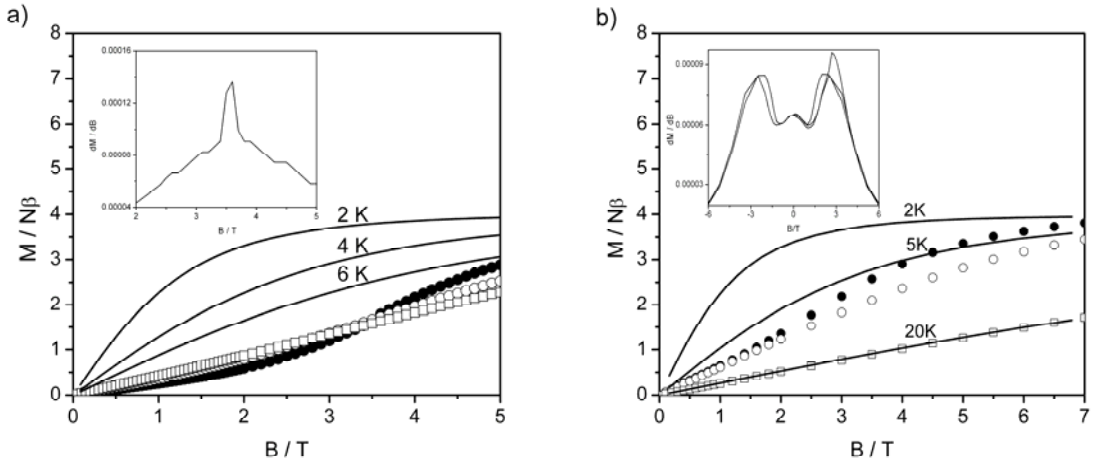

Figure 2.7. Plot of M/Nβ *vs* magnetic field for **1** (a) and **2** (b) in the range 0 to 5 (7) T at 2 (●), 4 (5) (○) and 6 (20) (□) K and the theoretical curves calculated with the Brillouin function assuming non-interacting spins $S = 2$. Inset, dM/dB *vs* B for **1** and **2** at $T = 2$K.

The experimental data in the range 12–20 K for **1** and 16–20 K for **2**, were least-square fitted with the equation (1) giving the parameters: a = 0.0013 $JK^{-4}mol^{-1}$, b = $-3.25\times10^{-6}JK^{-6}mol^{-1}$ and c = $3.01\times10^{-9}JK^{-8}mol^{-1}$ and a = 0.00168 $JK^{-4}mol^{-1}$, b = $-5.04\times10^{-6}JK^{-6}mol^{-1}$ and $c = 5.32\times10^{-9}JK^{-8}mol^{-1}$ for compounds **1** and **2**, respectively. The T^3 term can be interpreted in terms of the Debye model:

$$\frac{C}{R} = \frac{12\pi^4}{5}\left(\frac{T}{\Theta_D}\right)^3 \quad (2)$$

from which a Debye temperature, θ_D = 56 and 52 K is obtained for compounds **1** and **2**, respectively, which are typical values for this type of materials.[34] The magnetic heat capacities, C_m, obtained after subtracting the C_l as measured in zero applied field are displayed in Figure 2.8 for both compounds. The presence of broad maxima at temperatures 4.9 and 3.6 K for, respectively, compounds **1** and **2**, can be clearly distinguished by the heights of the maxima, amounting to about $C^{max}/R \approx 0.9$ for both. These maxima are interpreted as indicative of intrachain magnetic ordering. The much weaker anomalies observed around, *i.e.* 1.5 K and 1.4 K for compounds **1** and **2**, respectively, can be attributed to the establishment of long-range 3-D magnetic ordering between the chains, triggered by weak interchain magnetic coupling and likewise often observed in quasi-1-D magnetic materials.[33,35] Furthermore, by integrating C_m/T with respect to the temperature the magnetic entropy S_m can be obtained as a function of temperature (see insets in Figures 2.8a,b) and thus the total entropy change (ΔS_m) associated with the magnetic degrees of freedom can be

deduced. For compounds **1** and **2**, the experimental ΔS_m values in zero field are found to be: $\Delta S_m/R$ = 1.32 and 1.53, respectively, close to the theoretical value $\Delta S_m/R = \ln(2S+1) = \ln 5 = 1.60$ $JK^{-1}mol^{-1}$ expected for a spin $S = 2$ system (per mol of substance).

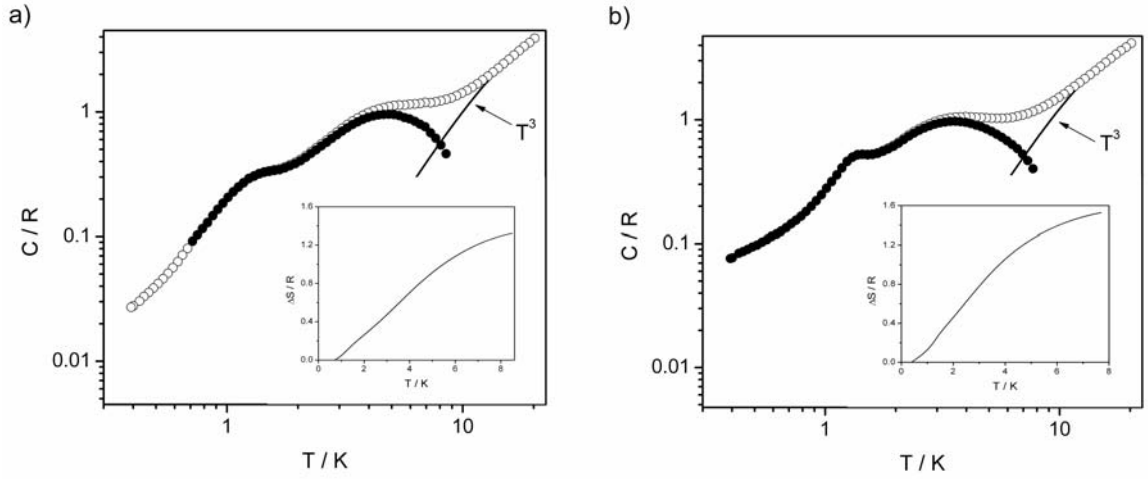

Figure 2.8. Total specific heat of compounds **1** (a) and **2** (b) measured in zero field. The estimated lattice contribution is shown by the solid curve. Dotted curves give the magnetic specific heat obtained after subtracting the phonon part. Inset, magnetic entropy curves obtained by integration of the data for compounds **1** and **2**.

From the positions of the maxima in the susceptibility (T_χ^{max}) and specific heat (T_C^{max}) a first rough estimate of the antiferromagnetic exchange constant J/k_B can be derived on basis of the predictions for the antiferromagnetic isotropic Heisenberg chain with $S = 2$.[33] With: $k_B T_\chi^{max}/|J| = 7.1$ and $k_B T_C^{max}/|J| = 4.25$, one obtains $J/k_B \approx 1$ K and 0.7 K for, respectively, compounds **1** and **2**. However, the observed height of the specific heat maximum is considerable larger than the value $C^{max}/R \approx 0.67$ predicted for this model.[33] Indeed, since magnetic compounds of manganese(III) usually show sizable crystal field anisotropy, with D/k_B of order 1–10 K,[36] a comparison with predictions for the anisotropic (antiferromagnetic) Heisenberg chain with $S = 2$ should be more appropriate. In the simplest case of uniaxial anisotropy the corresponding Hamiltonian for the chain reads:

$$H = -2J\sum_{i=1}^{n-1}\{S_i \cdot S_{i+1}\} + D\sum_{i=1}^{n} S_{iz}^2 \quad (3)$$

Depending on the sign of D, the anisotropy can be either of the Ising-type, when $D < 0$, or of the XY (planar) type for $D > 0$. Numerical calculations of the specific heat anomalies predicted on basis of Hamiltonian (equation 3) with $S = 2$ have been published by Blöte for both signs of D.[37] Unfortunately, predictions for the susceptibility of this model are not available. Therefore the susceptibility data of **1** and **2** are compared in Figure 2.6b with

predictions for the isotropic (D = 0) S = 2 Heisenberg model[38] and for the parallel susceptibility of the S = 2 Ising model (for which the antiferromagnetic interaction is only present between the z-components of the spins).[33] As can be seen in Figure 2.6b, the predictions for the position and the height of the susceptibility maximum are not too different for the two models, and for temperatures $k_BT/|J| > 15$ the theoretical curves coincide. Fitting the experimental data in the 20–40 K range to theory yields the values $J/k_B \approx 1.1$ K and 0.7 K for, respectively, compounds **1** and **2**. The experimental susceptibility maxima lie below the isotropic case, as expected for the powder susceptibility of a Heisenberg antiferromagnet with crystal field anisotropy, since the latter lowers the susceptibility in the hard direction(s). Similar estimates of the exchange constants have been obtained from the analysis of the specific heat maxima. Using the temperatures 4.9 and 3.6 K of these maxima found for, respectively, compounds **1** and **2**, one obtains $k_BT_C^{max}/|J| = 4.8$ and 4.0, respectively. The prediction by Blöte that comes closest to the experiments as regards position and height of the specific heat maximum is found to be the one with $|D/J| = 2$, with $D > 0$ (planar anisotropy) and $J < 0$ (antiferromagnetic). Although the prediction for $|D/J| = 2$ with $D < 0$ and $J < 0$ is not very different, it appears to decrease too fast in the temperature range below the maximum as compared to the experiment, see Figure 2.9 (the fast decrease is associated with the anisotropy gap in the energy spectrum induced by Ising-type anisotropy). In Figure 2.9 the data are compared to both these predictions, the fits yielding the same values as obtained from the susceptibility: $J/k_B \approx 1.1$ K and 0.7 K for compounds **1** and **2**, respectively. For comparison the predictions for the isotropic Heisenberg and the Ising chain models have been included. It can be clearly seen that the height of the specific heat maximum of the Ising model with $S = 2$ is much higher ($C^{max}/R \approx 1.5$) than the experiment, whereas that of the pure Heisenberg case is too low ($C^{max}/R \approx 0.67$). On basis of these results it is concluded that the magnetic anisotropy in **1** and **2** is not present in the magnetic exchange interaction, but arises instead from ligand field effects and is predominantly of planar symmetry. Obviously, on the basis of the present (powder) data it cannot be excluded that the symmetry is lower than uniaxial, for instance orthorhombic due to a substantial E-term. Therefore, HFEPR spectroscopic studies have been carried out to analyze the magnitude and symmetry of the zero-field splitting parameters (see Appendix A).

The behaviour of the field-dependent magnetization data, shown in Figure 2.7, confirms the above conclusions. Although ideally such measurements should be carried out on single crystals of the materials, powder data can still yield some valuable information. First, the comparison of the data with the Brillouin isotherms calculated for non-interacting spins S = 2, clearly confirms the presence of a substantial antiferromagnetic intrachain interaction, since the measured data fall much below the non-interacting limits. Second, for the anisotropic

Heisenberg antiferromagnet estimates of the antiferromagnetic exchange can be obtained from the saturation field, B_{sat}, measured at the lowest temperature. For the present purpose, the two comparisons can be approximately related by the equation $B_{sat} \approx 4z|J|S/g\beta$, bearing in mind that powder data are involved, *i.e.* the magnetization measured is an average over the different magnetic axes. Here z is the number of nearest magnetic neighbours ($z = 2$ for the chain). The magnetization curves taken at $T = 2$ K are seen to approach saturation for $B_{sat} \approx 7$ T for compound **2** (given that the saturation magnetization should correspond to 4 Nβ. For compound **1** an (extrapolated) value of about 9–10 T appears to be indicated. With $B_{sat} \approx 9$ T and 7 T, it is estimated that $J/k_B \approx -1.2$ K and -0.9 K for compounds **1** and **2** respectively, in agreement with the values derived from susceptibility and specific heat.

Furthermore, for both materials a discontinuity in the slope of the *M vs B* curves as measured at $T = 2$ K may be noted at critical fields $B_c \approx 3.6$ T and 2.5 T for, respectively, compounds **1** and **2**. This discontinuity is seen more clearly in the plots of the slope dM/dB *vs* field given in the insets of Figure 2.7. At higher temperatures ($>> z|J|/k_B$) the magnetization curve becomes linear, confirming that the discontinuity originates from the antiferromagnetic exchange. The effect could be due to a spin-flop phenomenon within the easy plane in case a weaker orthorhombic component E is present, imposing a preferential axis within this plane. However, more complicated field-induced transitions as may occur in more complex magnetic structures can of course not be excluded on basis of the present powder data.

As mentioned above, the small peaks observed in the specific heat of both compounds at approximately $T_c \approx 1.5$ K should correspond to the transition to 3-D long-range induced by the presence of weak interchain interactions, J'/k_B. The strength of these interchain couplings can be estimated from the ratio of T_c to the intrachain exchange J/k_B by a well known mean-field argument that runs as follows. In a system of weakly coupled chains, the 3-D ordering will occur at a temperature T_c at which the thermal energy, k_BT_c, equals the interaction energy between a given spin with a correlated chain segment in a neighbouring chain. Since the length of the correlated segment is proportional to the correlation length, the interchain ordering process is thus driven by the divergence of the intrachain correlation length ξ(T) as $T \rightarrow 0$. Then the value of T_c will be given by the expression:

$$k_BT_c/|J| = \xi(T_c)RS(S+1) \qquad (4)$$

where $R = |J'/J|$ is the ratio of inter- to intrachain exchange interactions. For the XY chain the temperature dependence of $\xi(T)$ is given by:

$$\xi(T) = 4|J|S(S+1)/k_BT_c \qquad (5)$$

therefore:

$$k_B T_c/|J| = 2S(S+1)(R)^{1/2} \quad (6)$$

The obtained R values are equal to 0.013 and 0.028 for compounds **1** and **2,** corresponding to $|J'|/k_B \approx 0.014$ K and 0.021 K, respectively. These values are of the order of the estimated magnetic dipolar interactions between neighbouring chains in these materials.

In summary, compounds **1** and **2** show antiferromagnetic behaviour as it is in fact expected for compounds in which superexchange is mediated through hydrogen bonds, since these are well known to mediate weak magnetic interactions.[39,40] For compound **1**, the maxima in χ_M and C_m are found at higher temperatures than for compound **2,** indicating a larger value of the magnetic superexchange interaction. The analysis of the magnetic specific heat data shows that a fit for compounds **1** and **2** is not possible, neither with the pure isotropic Heisenberg model, nor with the pure Ising antiferromagnetic chain models. Reasonable agreement was found with predictions for the anisotropic Heisenberg model with planar anisotropy for the antiferromagnetic $S = 2$ chain, the anisotropy originating from ligand field effects on the manganese(III) ion. Further studies have been performed with HFEPR spectroscopy, to confirm the sign and the magnitude of the anisotropy (see Appendix A). The temperature dependence of the specific heat also revealed the presence of long-range 3-D magnetic ordering between the chains below about 1.5 K for both compounds, probably induced by the weak interchain dipolar interactions.

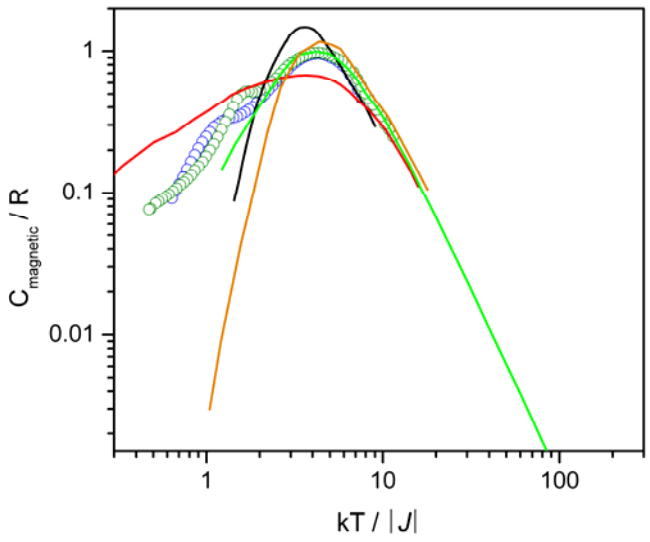

Figure 2.9. Comparison of the zero-field specific heat maximum for compounds **1** (blue circles) and **2** (green circles) with the predictions for the specific heat of the antiferromagnetic $S = 2$ chain for Heisenberg (red line), Ising (black line) and isotropic exchange interaction and positive D terms, $D/|J| = +2$ (light green line) and negative $D/|J| = -2$ (orange line), taken from Ref.37.

Compounds 3–6. Figure 2.10a shows no maximum in the χ_M *vs T* curve for both compounds **3** and **4**. Nevertheless, the magnetization data (Figure 2.11) taken at low temperature lie well below the calculated Brillouin curves for non-interacting spin $S = 2$ for both, indicating that antiferromagnetic intrachain interactions are likely to be present. In compound **3**, the $\chi_M T$ value stays almost constant down to about 20 K, where after it drops rather sharply. The deviations from the Brillouin curves are also smaller for this material than for **4**, suggesting that the antiferromagnetic intrachain interaction in **3** is quite weak and only becomes discernable below about 15 K. In compound **4**, the temperature dependence of χ_M and the behaviour of the magnetization suggest a stronger antiferromagnetic intrachain interaction. Compounds **3** and **4** form similar chain structures as compounds **1** and **2** where the N_2O_2 planes are parallel to each other in and between the chains. The most relevant structural difference is the increase of the distance between the manganese(III) ions along the chain imposed by the ligand H_2phpzMe. Consequently, antiferromagnetic interactions are weaker when compared with compounds **1** and **2**. Similar magnetic behaviour is observed for compounds **5** and **6**.

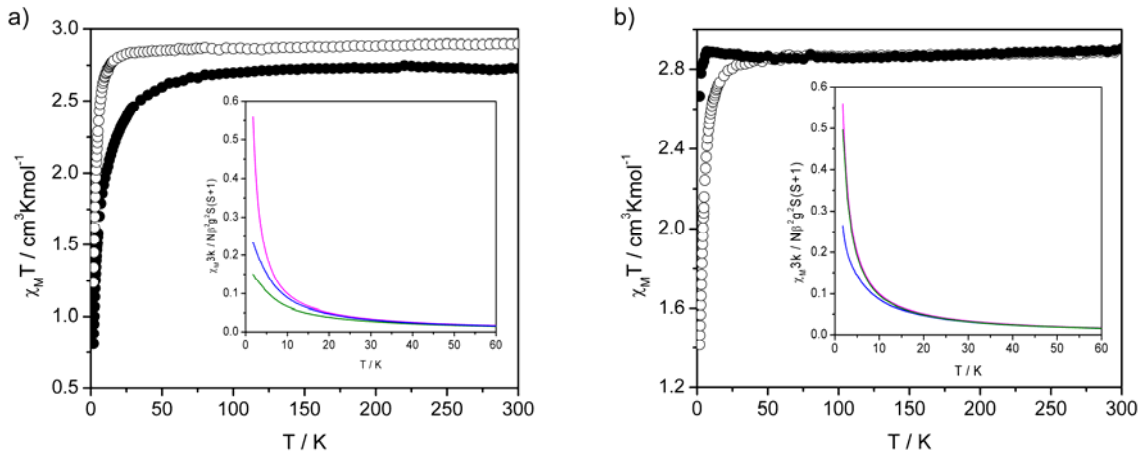

Figure 2.10. a) Plot of $\chi_M T$ *vs T* for **3** (○) and **4** (●) in the range 1.8 to 300 K in 0.1 T applied field. Inset, plot of χ_M *vs T* for **3** (blue) and **4** (green) with the paramagnetic behaviour (magenta). b) Plot of $\chi_M T$ *vs T* for **7** (○) and **8** (●) in the range 1.8 to 300 K in 0.1 T applied field. Inset, plot of χ_M *vs T* for **7** (blue) and **8** (green). The paramagnetic behaviour (magenta) just overlaps with the curve for **8** at all temperature range shown.

Compounds 7 and 8. The $\chi_M T$ value again remains almost constant down to about 30 K and 7 K for compounds **7** and **8**, respectively (Figure 2.10b). The temperature dependence of χ_M for compound **7** lies below the paramagnetic behaviour, while that of compound **8** overlaps with it. The low-temperature magnetization curves given in Figure 2.12, indicate the

presence of weak antiferromagnetic interactions in **7** (similar in strength as in **4**), whereas compound **8** basically behaves as a paramagnet.

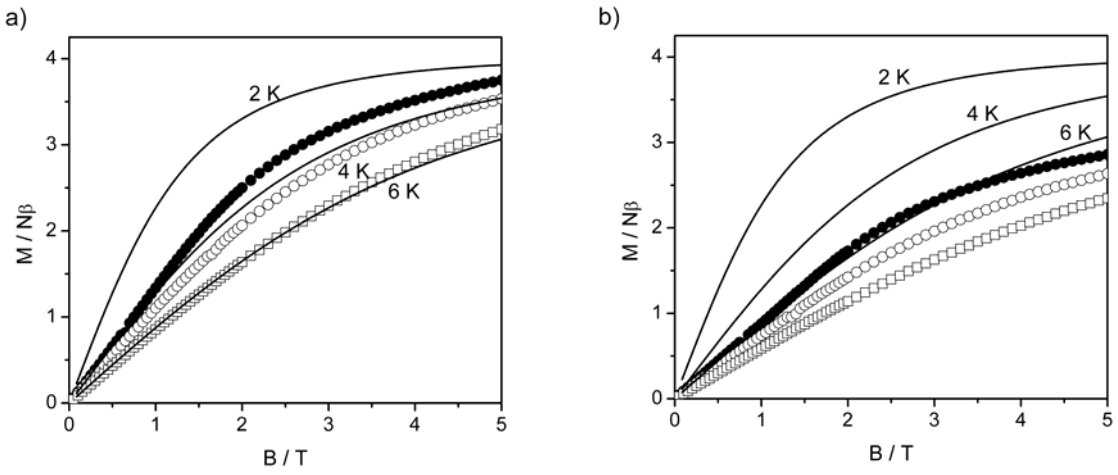

Figure 2.11. Plot of M/Nβ *vs* magnetic field for **3** (a) and **4** (b) in the range 0 to 5 T at 2 (●), 4 (○) and 6 (□) K and the theoretical curves calculated with the Brillouin function assuming one non-interacting spin $S = 2$.

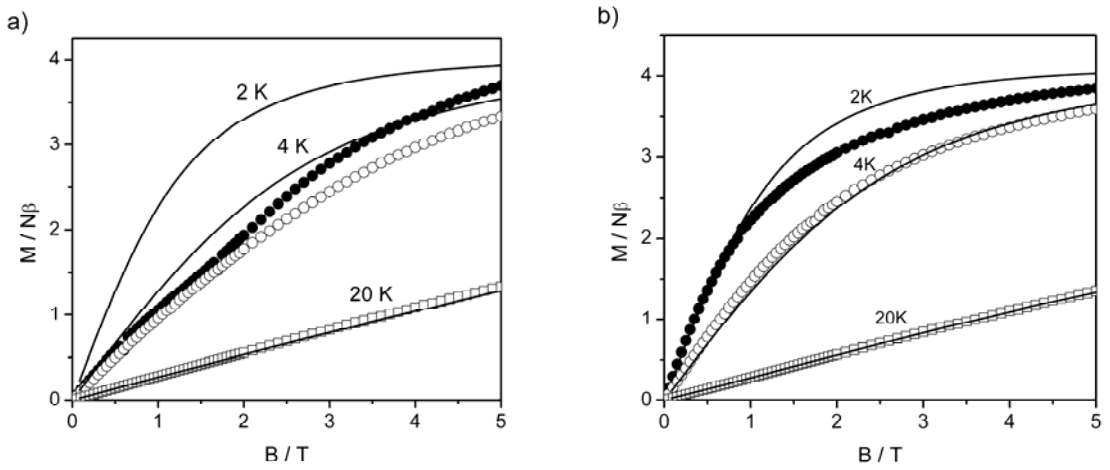

Figure 2.12. Plot of M/Nβ *vs* magnetic field for **5** (a) and **6** (b) in the range 0 to 5 T at 2 (●), 4 (○) and 20 (□) K and the theoretical curves calculated with the Brillouin function assuming one non-interacting spin $S = 2$.

2.4. Conclusions

A family of five-coordinated manganese(III) compounds with the general formula $[Mn(HphpzR)_2X]$ (R = H, Me, Et, Ph and X^- = Cl^-, Br^-) (**1–8**), has been synthesized and characterized. In compounds **1–8**, the square-pyramidal geometry is thermodynamically favoured above the well known octahedral-based geometry for a manganese(III) ion, probably due to the formation of the neutral molecular compounds.[30] Nevertheless, a complex with octahedral geometry can also be formed in the presence of an excess of ligand as illustrated by the formation of compound **9** that was only characterized crystallographically. The type and the strength of magnetic interactions between manganese(III) ions have been studied by changing the ligand and the type of halogen coordinated to the manganese(III) ion. From the X-ray crystallographic studies, it can be seen that the presence of various substituents on the pyrazole ring of the ligand does neither significantly modify the coordination geometry of the metal ion, nor the coordination mode of the ligand. However, the steric effects of the ligand side groups result in a difference in the crystal packing of the compounds. Compounds **1–4** form ladder-like chains as a result of the intermolecular hydrogen bonding interactions, while compounds **7** and **8** are isolated mononuclear units arranged in a face-to-face manner that form hydrogen bonds only with the solvent molecules. The observed differences in the crystal packing, as well as the distance between the manganese(III) ions, appear to be essential in determining the type and the strength of the magnetic interactions. Compounds **1** and **2** show antiferromagnetic short-range interactions between the manganese(III) ions. Specific heat measurements confirm the presence of 1-D short-range correlations and long-range magnetic ordering below 1.5 K. Compounds **3–8** exhibit weaker antiferromagnetic interactions. In these cases, the strength of the magnetic interactions is smaller due to the steric hindrance of the ligand that separates the manganese(III) ions. This family of compounds proves that small structural differences can strongly influence the magnetic properties. Some of the compounds described here have been used as building blocks for the synthesis of higher nuclearity compounds that will be discussed in the following chapters (Chapter 3 and 5).

2.5. References

1. Aromí, G.; Brechin, E. K., *Struc. Bond.,* **2006**, 122, 1-67.
2. Christou, G.; Gatteschi, D.; Hendrickson, D. N.; Sessoli, R., *MRS Bull.,* **2000**, 25, 66-71.
3. Gatteschi, D.; Sessoli, R., *Angew. Chem.-Int. Edit.,* **2003**, 42, 268-297.
4. Wernsdorfer, W.; Aliaga-Alcalde, N.; Hendrickson, D. N.; Christou, G., *Nature,* **2002**, 416, 406-409.
5. Miyasaka, H.; Saitoh, A.; Abe, S., *Coord. Chem. Rev.,* **2007**, 251, 2622-2664.
6. Lecren, L.; Wernsdorfer, W.; Li, Y. G.; Vindigni, A.; Miyasaka, H.; Clérac, R., *J. Am. Chem. Soc.,* **2007**, 129, 5045-5051.
7. Kachi-Terajima, C.; Miyasaka, H.; Sugiura, K.; Clérac, R.; Nojiri, H., *Inorg. Chem.,* **2006**, 45, 4381-4390.

8. Ajò, D.; Bencini, A.; Mani, F., *Inorg. Chem.,* **1988**, 27, 2437-2444.
9. Tanase, S.; Koval, I. A.; Bouwman, E.; De Gelder, R.; Reedijk, J., *Inorg. Chem.,* **2005**, 44, 7860-7861.
10. Mukherjee, R., *Coord. Chem. Rev.,* **2000**, 203, 151-218.
11. Tanase, S.; Aromí, G.; Bouwman, E.; Kooijman, H.; Spek, A. L.; Reedijk, J., *Chem. Commun.,* **2005**, 3147-3149.
12. Tanase, S.; Bouwman, E.; Long, G. J.; Shahin, A. M.; Mills, A. M.; Spek, A. L.; Reedijk, J., *Eur. J. Inorg. Chem.,* **2004**, 4572-4578.
13. Viciano-Chumillas, M.; Tanase, S.; Aromí, G.; Smits, J. M. M.; de Gelder, R.; Solans, X.; Bouwman, E.; Reedijk, J., *Eur. J. Inorg. Chem.,* **2007**, 2635-2640.
14. Mozingo, R., *Org. Synth.,* **1941**, 21, 42-44.
15. Sequin, U., *Helv. Chim. Acta,* **1981**, 64, 2654-2664.
16. Wheeler, T. S., *Org. Synth.,* **1952**, 32, 72-76.
17. Addison, A. W.; Burke, P. J., *J. Heterocycl. Chem.,* **1981**, 18, 803-805.
18. Kahn, O., *Molecular Magnetism*. Wiley-VCH: New York, 1993.
19. Sheldrick, G. M. *Program for Emperical Absorption Correction*, University of Göttingen, Germany: 1996.
20. Beurskens, P. T.; Beurskens, G.; Strumpel, M.; Nordman, C. E., *in Patterson and Pattersons*. Glusker, J. P.; Patterson, B. K.; Rossi, M., Eds. Clarendon Press: Oxford: 1987.
21. Duisenberg, A. J. M.; Kroon-Batenburg, L. M. J.; Schreurs, A. M. M., *J. Appl. Crystallogr.,* **2003**, 220-229.
22. Duisenberg, A. J. M. Reflections on area detectors. PhD thesis, Utrecht, 1998.
23. Beurskens, P. T.; Beurskens, G.; Bosman, W. P.; De Gelder, R.; García-Granda, S.; Gould, R. O.; Israël, R.; Smits, J. M. M.; Smykalla, C. *The DIRDIF96. A computer program system for the crystal structure determination by Patterson methods and direct methods applied to difference structure factors*, Crystallography Laboratory, University of Nijmegen: Nijmegen, The Netherlands, 1996.
24. Sheldrick, G. M. *SHELXS-97: Program for Crystal Structures Determination*, University of Göttingen; Germany: Göttingen, 1997.
25. Sheldrick, G. M. *SHELXL-97: Program for the Refinement of Crystal Structures*, University of Göttingen; Germany: Göttingen, 1997.
26. Nakamoto, K., *Infrared and Raman Spectra of Inorganic and Coordination Compounds*. 4th ed ed.; John Wiley & Sons Inc 1997.
27. Lever, A. B. P., *Inorganic Electronic Spectroscopy*. Elsevier: Amsterdam, 1997.
28. Godbole, M. D.; Grigiotti, E.; Zanello, P.; Mills, A. M.; Spek, A. L.; Bouwman, E., *Inorg. Chim. Acta,* **2005**, 358, 233-238.
29. Viciano-Chumillas, M.; Tanase, S.; Mutikainen, I.; Turpeinen, M.; de Jongh, L. J.; Reedijk, J., *Inorg.Chem.,* **2008**, 47, 5919-5929.
30. Katsuki, T., *Coord. Chem. Rev.,* **1995**, 140, 189-214.
31. Addison, A. W.; Rao, T. N.; Reedijk, J.; Vanrijn, J.; Verschoor, G. C., *J. Chem. Soc.-Dalton Trans.,* **1984**, 1349-1356.
32. Carlin, R. L., *Magnetochemistry*. Springer-Verlag: Berlin, 1986.
33. de Jongh, L. J.; Miedema, A. R., *Adv. Phys.,* **2001**, 50, 947-1170.
34. Evangelisti, M.; Luis, F.; de Jongh, L. J.; Affronte, M., *J. Mater. Chem.,* **2006**, 16, 2534-2549.
35. Granroth, G. E.; Meisel, M. W.; Chaparala, M.; Jolicoeur, T.; Ward, B. H.; Talham, D. R., *Phys. Rev. Lett.,* **1996**, 77, 1616-1619.
36. Boča, R., *Coord. Chem. Rev.,* **2004**, 248, 757-815.
37. Blote, H. W. J., **1975**, 79, 427-466.
38. Weng, C. H. PhD thesis, Carnegie-Mellon University, Pittsburg, PA, 1968.
39. Delgado, F. S.; Kerbellec, N.; Ruiz-Pérez, C.; Cano, J.; Lloret, F.; Julve, M., *Inorg. Chem.,* **2006**, 45, 1012-1020.
40. Desplanches, C.; Ruiz, E.; Rodríguez-Fortea, A.; Alvarez, S., *J. Am. Chem. Soc.,* **2002**, 124, 5197-5205.